

Gaia Data Release 1

Validation of the photometry

D. W. Evans¹, M. Riello¹, F. De Angeli¹, G. Busso¹, F. van Leeuwen¹, C. Jordi², C. Fabricius², A. G. A. Brown⁴, J. M. Carrasco², H. Voss², M. Weiler², P. Montegriffo³, C. Cacciari³, P. Burgess¹, and P. Osborne¹

¹ Institute of Astronomy, University of Cambridge, Madingley Road, Cambridge CB3 0HA, UK
e-mail: dwe@ast.cam.ac.uk

² Institut de Ciències del Cosmos, Universitat de Barcelona (IEEC-UB), Martí Franquès 1, 08028 Barcelona, Spain

³ INAF–Osservatorio Astronomico di Bologna, via Ranzani 1, 40127 Bologna, Italy

⁴ Sterrewacht Leiden, Leiden University, PO Box 9513, 2300 RA Leiden, The Netherlands

Received 4 July 2016 / Accepted 8 January 2017

ABSTRACT

Aims. The photometric validation of the *Gaia* DR1 release of the ESA *Gaia* mission is described and the quality of the data shown.

Methods. This is carried out via an internal analysis of the photometry using the most constant sources. Comparisons with external photometric catalogues are also made, but are limited by the accuracies and systematics present in these catalogues. An analysis of the quoted errors is also described. Investigations of the calibration coefficients reveal some of the systematic effects that affect the fluxes.

Results. The analysis of the constant sources shows that the early-stage photometric calibrations can reach an accuracy as low as 3 mmag.

Key words. catalogs – surveys – instrumentation: photometers – techniques: photometric – Galaxy: general

1. Introduction

The photometric calibration of the first data release of the *Gaia* catalogue ([Gaia Collaboration 2016a](#)) aims to achieve mmag-level precision ([van Leeuwen et al. 2017](#)). This is carried out via an internal, self-calibrating method as detailed in [Carrasco et al. \(2016\)](#). No comparison with a set of standards would be sufficient to confirm that the accuracies quoted for the photometry were valid because the precision aimed for is better than the precision of other currently available large catalogues of photometric standards. Also, unexpected systematic effects have been found in the *Gaia* data that required additional calibrations to be carried out with respect to the initial plan (Riello et al., in prep.), such as linear trends with time and increased background level. It is necessary to check that these calibrations have removed all the systematic effects and that the accuracies achieved are close to the photon noise level. It is expected that future releases of the *Gaia* catalogue will have improved accuracies as further calibrations are introduced into the data processing.

Although no colour nor spectral information is included in this data release, some validation is given to the processing of the spectral calibrations of blue and red photometers (BP and RP, respectively). This is due to the use of colour information in the calibration of the *G*-band photometry, which is itself internally calibrated. We also present some results of the validation of the epoch photometry available in the *Gaia* EPSL release ([Eyer et al. 2016](#)).

Sections 3 to 6 of this paper cover the direct validations of the calibrations carried out in the photometric processing. This is followed by internal consistency checks using the accumulated photometric data, the photometric residuals, and an analysis of

the epoch photometry of constant sources in Sects. 7–9. External comparisons are then described in Sect. 10. Finally, Sect. 11 summarises the conclusions. Appendix A contains a list of the acronyms used in this paper.

Further validation of the overall catalogue can be found in [Arenou et al. \(2017\)](#).

The following subsection provides a brief description of the *Gaia* instruments and data. Many more details are available from [Gaia Collaboration \(2016b\)](#).

2. Input data

Gaia is a scanning satellite. The full sky is expected to be covered in about six months of observations, but the number of observations per source largely depends on the astrophysical coordinates of the source.

The main input data for the photometric processing comes from the astrometric field (AF) CCDs. This is an array of seven rows (parallel to the along-scan (AL) direction) and nine strips (parallel to the across-scan (AC) direction) of CCDs collecting light in the *Gaia* *G* broad band. Colour information for each source (also a fundamental ingredient for the photometric calibrations) is derived from the low-resolution spectra collected by the BP and RP instruments. The light is dispersed in the along-scan direction.

In the following we will refer to field-of-view (FoV) and CCD transits: a FoV transit includes several CCD transits (usually nine AF, one BP, and one RP CCD transit). It should be noted that the two FoVs are simultaneously projected onto the focal plane array.

Only small windows centred on the detected sources are downloaded from the satellite. The size of these windows depends on the magnitude estimated on board; only bright sources are observed with 2D windows. Different configurations are referred to as “window classes”. The shape of the windows (normally rectangular) can be complicated by conflicts between adjacent sources in crowded regions in the sky. These non-nominal cases have not been treated yet and have not contributed to the photometry published in *Gaia* DR1.

The CCDs are operated in a time-delayed integration (TDI) mode whereby charges are integrated while they move across the CCD. The effective exposure time over one CCD is approximately 4.5 s, but this can be reduced by activating the “gates”. Several different gate configurations are defined and a particular gate is assigned to each CCD transit depending on the magnitude of the source as estimated from the strip of CCD preceding the AF (known as the “star mapper” or SM CCDs) and the AC position of the source in the focal plane. Over a FoV transit, different gate configurations can be used on individual CCD observations. The activation of a gate triggered by the transit of a bright source, will affect all other sources observed simultaneously in the same region of a CCD. It may also affect only part of a window, thus creating complex gate cases that have not yet been treated by the photometric processing.

Different gate and window class configurations effectively define different instruments (referred to as calibration units) that need to be calibrated to form one consistent reference system (for more details see [Carrasco et al. 2016](#)).

The input data to the photometric processing consists of image parameters (such as fluxes, centroids, and goodness of fit measurements) for the SM and AF CCD transits, and raw BP and RP spectral data. Errors on the *G*-band flux measurements are estimated in the image parameter determination (IPD) process; for more details refer to [Fabricius et al. \(2016\)](#).

Two significant and unexpected features were discovered during the commissioning period and required the introduction of ad hoc calibrations. One is the presence of stray light scattered by the solar shield, causing the background level to be up to two orders of magnitude higher than expected (with large variations depending on the rotation phase of the satellite). The additional stray light component of the background can be calibrated, but the associated noise will affect performance for faint objects. The other feature is a decrease over time of the throughput of the instruments due to continued contamination by water ice. The wavelength-dependent transmission loss is different for the two FoVs and varies across the focal plane. This adds a systematic effect to the photometric data that is orders of magnitude larger than expected and in particular affects our ability to create a consistent reference catalogue for the internal calibration. An additional calibration of this strong time dependency in the transmission had to be included to solve this problem.

3. Validation of BP/RP spectral calibrations

Even though colour information is not included in *Gaia* DR1, BP and RP data are processed to produce the colour information required to calibrate the *G*-band photometry. This section focusses on the validation of the along-scan geometric calibration of the spectrophotometric data. This is a fundamental element in the computation of colour information in the form of spectrum shape coefficients (SSC; see [Carrasco et al. 2016](#)). The application of this calibration and of the nominal dispersion function brings all the data onto the same wavelength system.

The BP/RP windows that are assigned on board will generally not be well centred on the source. This is expected, given the design of the instrument, and is due to various factors: the location of the centroid from the SM observation may not be very accurate, and sources may have a non-negligible motion along or across scan. This implies that considering an arbitrary reference wavelength, the location will not correspond to the same location in sample space even in spectra of the same source (for a definition of sample space see [Gaia Collaboration 2016b](#)).

The location of the centre of the source, or more precisely of a reference wavelength in the dispersed image of the source, can be predicted by extrapolation from the series of source centroids of each of the AF observations that precede the BP/RP observations in a FoV transit. However, this requires an accurate knowledge of the geometric calibration of the BP/RP CCDs with respect to the AF CCDs (and of the satellite attitude).

To calibrate the geometry of the instrument, this prediction needs to be compared to the actual location of the reference wavelength in the observed spectra. This is done by selecting a small fraction of the observed spectra based on a filter in colour and magnitude, so that we can be confident that we are using spectra of sources with a similar spectral energy distribution, where the sample position corresponding to the reference wavelength will be the same (except for the effect of non-perfect centring of the window mentioned above) and that we are filtering observations with a high signal-to-noise ratio. The colour range adopted is [0.3, 0.6] for the calibration of the BP instrument and [1.3, 1.6] for the calibration of the RP one. These correspond approximately to spectral types F and K (based on nominal knowledge of the instrument and pre-launch simulations). This colour selection, in addition to other filters designed to select isolated spectra and to avoid spectra that are affected by cosmic rays, yields a sufficient number of calibration spectra. This is of the order of several hundreds for each calibration unit of the large-scale component of the AL geometric calibration model which is the one that is updated most often (every 20 OBMT revolutions or about 5 days for *Gaia* DR1). The selected spectra are aligned and used to generate a reference spectrum, which is then fitted back to each spectrum to evaluate the sample position of the reference wavelength within the actual sampling. Two reference spectra are defined for the entire dataset, one for BP and one for RP.

At this stage, the processing has concentrated on differential calibrations of the various instrument configurations onto the same internal reference system. This is then tied to the absolute system adopting the nominal pre-launch knowledge of the instrument. In this simplified schema, it is acceptable to adopt as the reference wavelength the nominal value which corresponds to the central sample of a perfectly centred window and to assume that the reference spectrum (being the result of an accumulation over an extremely large number of observed spectra) will be representative of a perfectly centred spectrum.

The geometric calibration model is defined by the following components (for more details see [Carrasco et al. 2016](#)):

- a large-scale component, computed over a short timescale, defined by a linear combination of shifted Legendre polynomials describing overall effects of translation, rotation, and curvature;
- an offset for different gate configurations (relative to the ungated case) computed on a longer timescale, taking into consideration the residual effects;
- an offset for different CCD AC stitch blocks, also computed on a long timescale, taking into account the effects due to

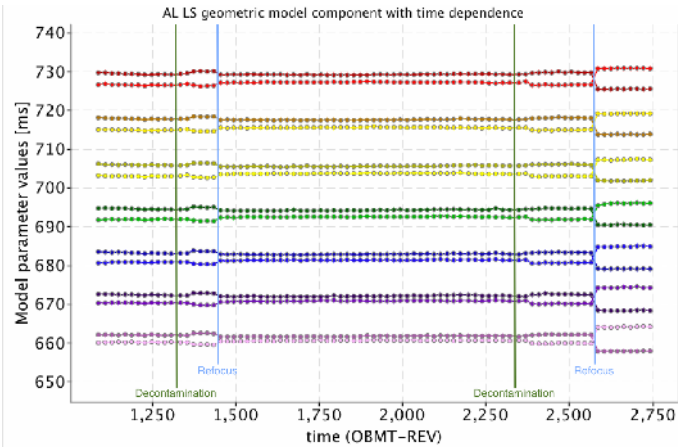


Fig. 1. Evolution in time of the zeroth-order coefficients of the large-scale component of the BP geometric calibration. The units on the ordinate axis are ms (the TDI period is 1 ms). The units on the abscissa axis are OBMT revolutions (one revolution corresponds to approximately 6 h). The OBMT range covers the entire science acquisition period for *Gaia* DR1, i.e. between 25 July 2014 and 16 September 2015. Different colours are used to indicate different CCD rows (CCD rows 1 to 7 from red to violet, lighter colours for the preceding field of view, darker ones for the following field of view). Each large-scale calibration covers a time range of about 20 revolutions (5 days).

the photolithography process used to manufacture the CCDs (for more details on the definition of the stitch blocks see [Gaia Collaboration 2016b](#)).

Sudden variations in the values of the calibration coefficients over time should only take place corresponding to particular and known satellite events or features/changes in the input data produced by the upstream systems. Therefore, the main validation analysis is based on the temporal evolution of the calibrations. Figure 1 shows the evolution versus time (in OBMT revolutions, where one revolution lasts approximately 6 h; see [Gaia Collaboration 2016b](#)) of the zeroth order coefficients in the large-scale component. Some known events are marked in the plot using vertical lines (two decontamination activities in dark green and two refocus activities in blue). As expected, these significantly affect the calibrations. Decontamination activities were introduced to mitigate the problem of contamination affecting mirrors and CCDs. During these activities, the mirrors and CCDs were heated. The decontamination and refocus activities mainly affect the basic angle, while they seem to have an almost negligible effect on the relative geometry of AF and BP/RP.

It is interesting to note that the variations following a decontamination seem to take place with some delay. This is likely due to the fact that data collected just after a decontamination event are not of sufficient quality to generate an updated AF geometric calibration, and therefore this update takes place only once the entire instrument has cooled down sufficiently. Variations in the level of the BP/RP geometric calibration coefficients are expected whenever a new geometric calibration for the AF field comes in place. This occurs because the extrapolation of the AF centroids to the BP/RP CCDs depends on the AF geometric calibration.

As can be seen from Fig. 1, the large-scale component is very stable over stretches of nominal operations.

Figure 2 shows the time evolution of the first- and second-order large-scale coefficients. The colour-coding is the same as

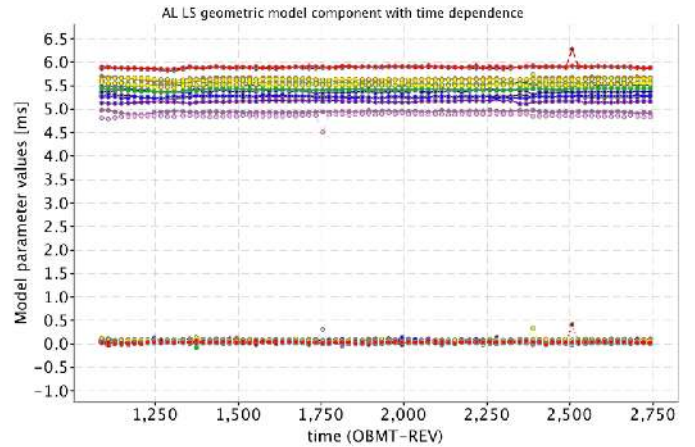


Fig. 2. Evolution in time of the first- (distributed between 4.5 and 6 ms) and second-order coefficients (distributed between -0.5 and 0.5 ms) of the large-scale component of the BP geometric calibration. The units on the ordinate axis are ms. The units on the abscissa axis are OBMT revolutions (one revolution corresponds to about 6 h). The OBMT range covers the entire science acquisition period for *Gaia* DR1. Colour-coding is as in Fig. 1.

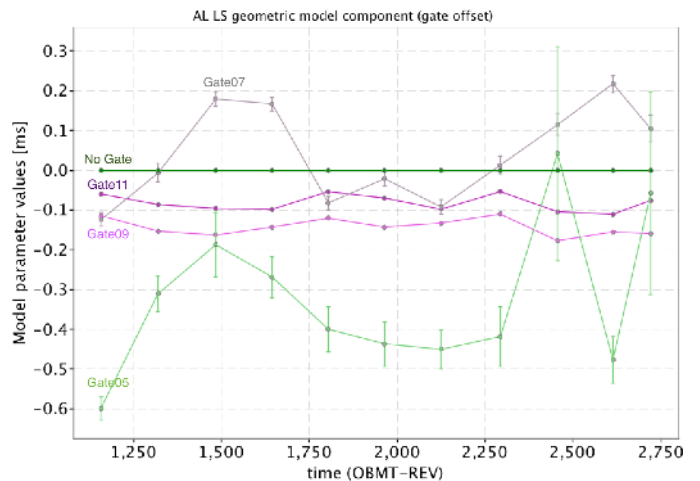


Fig. 3. Evolution in time of the gate offset coefficients of the large-scale component of the BP geometric calibration. The units on the ordinate axis are ms. The units on the abscissa axis are OBMT revolutions (one revolution corresponds to about 6 h). The OBMT range covers the entire science acquisition period for *Gaia* DR1. Different colours are used to indicate different gate configurations as indicated by the labels.

in Fig. 1. The second-order coefficients are always very close to 0. Both sets of coefficients are quite stable.

Finally, Fig. 3 shows the offset calibrated for different gate configurations. The only gates that could be calibrated over the whole period are Gate09, Gate11, Gate07, and Gate05. The coefficients for Gate05 and Gate07 are quite noisy (the width of the distribution of the parameter values for these two configurations is 0.22 and 0.14 pixels to be compared with 0.02 obtained for both Gate09 and Gate11). This is due to the small amount of data available for these calibrations. Time ranges covering about 160 revolutions (40 days) were used for this run of the gate offset calibration. Longer time ranges could be adopted in future runs if the calibrations are sufficiently stable.

The final set of coefficients, calibrating small-scale effects on the scale of CCD AC stitch block, produces offsets that are

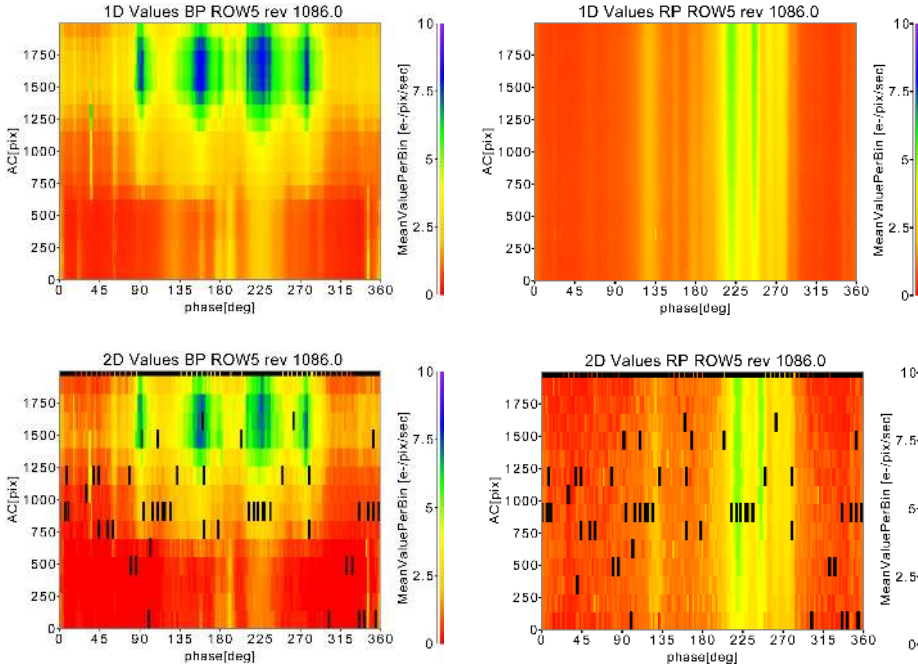


Fig. 4. Stray light discrete maps for BP and RP in the *left and right plots*, respectively, built with 1D observations (see text for details). In abscissa is the spin phase and in ordinate the AC coordinate. The bin values in electron/pixel/s are colour-coded as in the bar to the left. Rev time in the figure label indicates the start of the time range when the data were acquired, in this case revolution 1086.

always below 0.05 pixel in absolute value and are quite stable (the width of the distribution over time of these parameters is lower than 0.02 pixels in every calibration unit).

The validation of the geometric calibrations is primarily based on the analysis of the standard deviation of the single calibrations. The standard deviation of the zeroth-order parameter for each single calibration unit, over the 6 months following the first refocus event, is of the order of 0.06 ms for BP (equivalent to 0.06 pixel or 0.5 nm in terms of wavelength) and 0.15 ms for RP (i.e. 0.15 pixel or 1.65 nm in terms of wavelength). Errors of this size are negligible when computing the spectrum shape coefficients used for the photometric calibrations. This is the only relevant quantity for *Gaia* DR1 as spectral data is not yet included in the release.

It should be noted that systematic errors on the geometric calibration parameters would not affect the photometric calibrations as they will simply result in a slightly different set of SSC bands being used for the definition of the colour information.

The RP results (not shown in this paper) are equivalent to the BP ones.

4. Validation of BP/RP stray light calibration

As described in Riello et al. (in prep.) the current implementation of the background correction takes into account only the stray light calibration as it is the most important contribution to the background. As Carrasco et al. (2016) have noted, this correction of the stray light also includes the smoother component of the astrophysical background. The stray light is modelled as a discrete 2D map, obtained by accumulating eight revolutions of data (corresponding to roughly 2 days). The map coordinates are the heliotropic coordinate spin phase and the AC coordinate. The 1D and 2D transits are processed separately because analysis of the data shows that while the structure of the map is very similar, there is a small offset (still under investigation) between the two. Since there are many more 1D transits than 2D transits, they have a much higher weight in the determination of the bin values, and using a map built with both kinds of observations

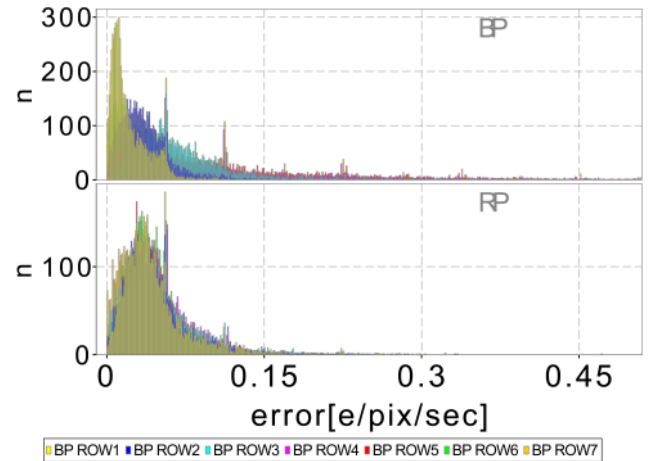


Fig. 6. Error distribution (in electron/pixel/s) for the stray light maps built with 1D observations (colour-coded by CCD row). *Top*: BP. *Bottom*: RP.

leads to an overcorrection when removing the background for the 2D transits. The amplitude of this offset depends on the CCD and varies between 0 and 2 electron/pixel/s. This does not affect the photometry because it is calibrated out by creating separate maps for 1D and 2D windows. In addition, the grid used to build the maps for 1D and 2D transits are different, with 360 bins in phase and 20 in AC coordinate in the former and 180 and 15 in the latter. This allows fewer empty bins for the maps built with 2D transits.

Examples of stray light maps obtained with 1D transits for BP and RP are shown in Fig. 4, while maps obtained with 2D transits are shown in Fig. 5.

A first validation is done directly by inspecting the map and looking at the distribution of the errors. The value in a bin is the median value obtained from all observations contributing to the bin. The median was chosen instead of the mean to reduce the effect of outliers caused for instance by cosmic rays or contamination from stars. The error for a bin is calculated as the median absolute deviation (MAD) associated with the median

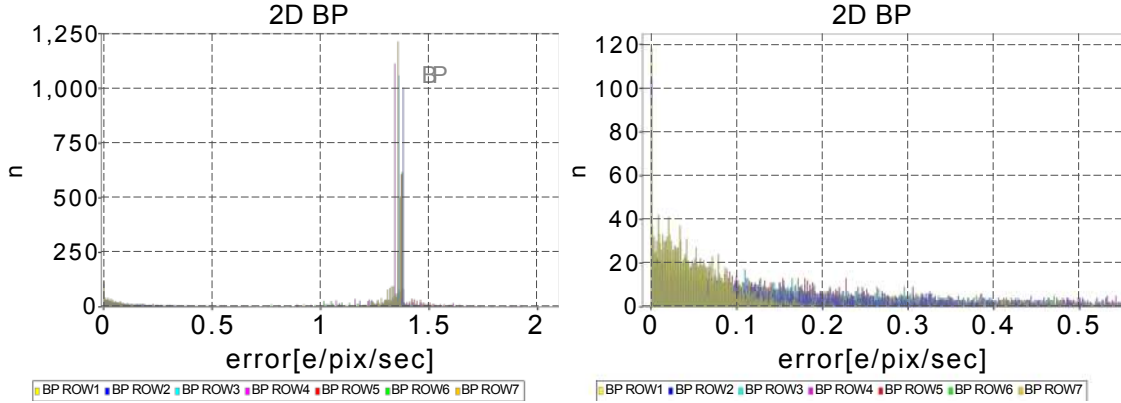


Fig. 7. Error distribution (in electron/pixel/s) for the stray light maps built with 2D observations for BP (colour-coded by CCD row). The *plot on the left* shows all data, while the one on the *right* contains only the error values for the map bins with more than one measurement. See text for details.

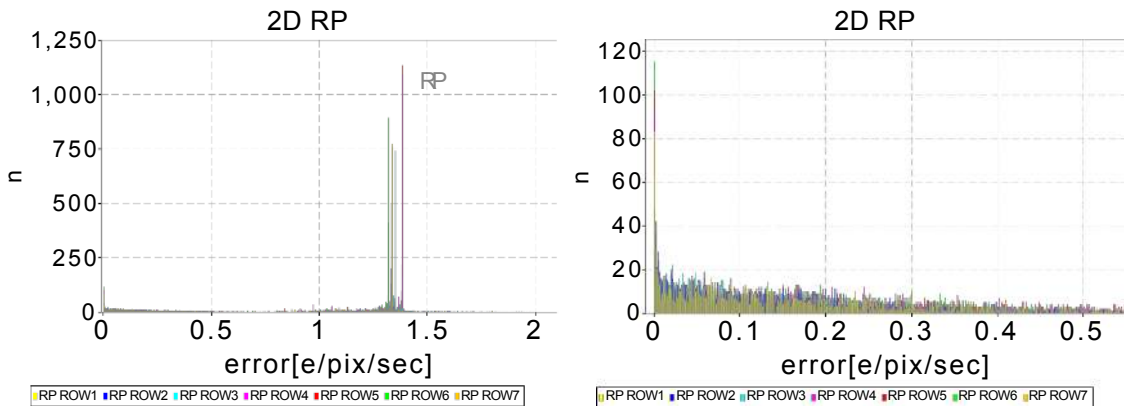


Fig. 8. As in Fig. 7 for RP.

value. Figures 6–8 show the histograms for the stray light map bin errors, with a histogram bin size of 0.001 (electron/pixel/s). For the maps obtained with the 1D transits, the distributions are broadly similar for all CCDs. However, while in RP there is a close similarity between the rows, in BP there are more differences; this is explained by the fact that in RP the stray light features are similar for all CCDs, while in BP the features can change significantly in shape, position, and strength. For the maps obtained with the 2D transits, it is evident that there are two distributions: the first between 0 and 0.05, very similar to that for 1D transits and the second between 1.35 and 1.4. The latter is due to the stray light bins with only one measurement, so that the error in that case is not the error on the median but the error on that single measurement.

The residuals obtained by subtracting the map from the same data used to calculate it have also been analysed. Figure 9 shows examples of residual histograms. The histograms were normalised to the same area to allow a better comparison. The distribution is well centred around zero, with a different width for 1D and 2D transits, showing that the model is correct and that there is no residual trend.

An additional check is the calculation of the scatter of the residuals, made using an interquartile method used in the HIPPARCOS mission (ESA 1997) which uses the percentile values at 15.85 and 84.15% to robustly estimate the standard deviation of the distribution (see also Sect. 9). The scatter is lower for 1D than 2D observations, as shown in Fig. 9 (left panel) where the value is ~ 0.053 electron/pixel/s for residuals from 1D observations, while it is ~ 0.131 electron/pixel/s for residuals from 2D observations. This is expected, since for 2D windows the number

of observations is much lower (about 10% of the number of 1D windows) and therefore the model is less accurate and the residuals are bigger. The same results apply to RP as well. The worst case, shown in the right panel of Fig. 9, is when the variations in the AC and AL directions are quite large, but this is expected as well since the resolution of the map is not sufficient to reproduce the rapid variations. Unfortunately, increasing the resolution of the map is not an option because there is simply not enough data available to robustly measure the background level. This scatter translates into an error in magnitude which is well below the expected end-of-mission error: in the worst case, the values are comparable but it should be noted that the end-of-mission error is calculated based on the accumulation of the measurements, while the scatter is calculated on single measurements and will decrease.

5. Study of LS and SS calibration coefficients

As described in Carrasco et al. (2016), two of the main photometric calibrations are referred to as the large-scale (LS) and small-scale (SS) calibrations. They can be used for validation in two ways. The first is used in the validation of the calibrations themselves, and the second is used in the validation of the photometry as a whole in the detection of anomalies.

When the calibrations are carried out, the unit-weight standard deviation of the solution is calculated. This is defined as the square root of the normalised chi-square (van Leeuwen 2007). This gives an indication of how well the solution model is able to remove any systematic effects. In the ideal case, this value should be around 1.0. However, in these early stages of the mission,

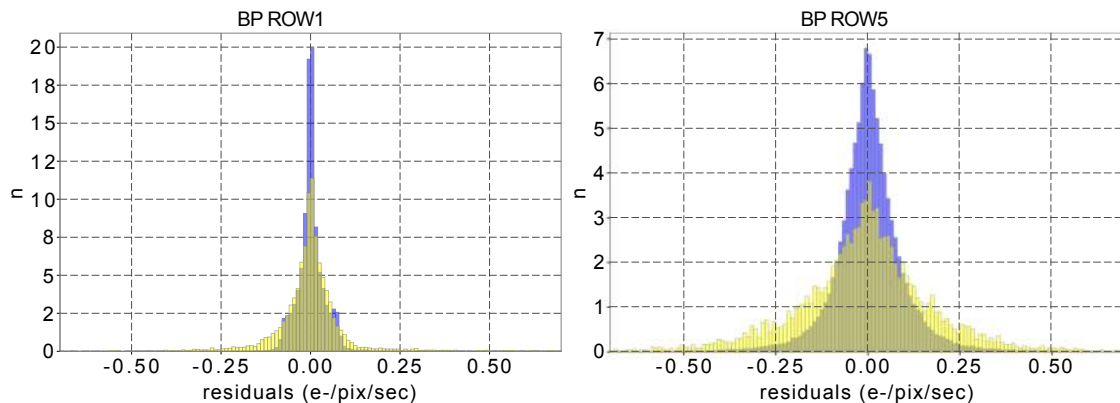


Fig. 9. Residual distribution (normalised to the same area) for the stray light maps. In blue the data obtained from 1D transits, in yellow from 2D transits. The *left plot* shows the best case (for BP ROW1 with scatter ~ 0.031 for 1D data and ~ 0.057 for 2D data), while the *right plot* shows the worst case (for BP ROW5, with scatter ~ 0.075 for 1D data and ~ 0.161 for 2D data).

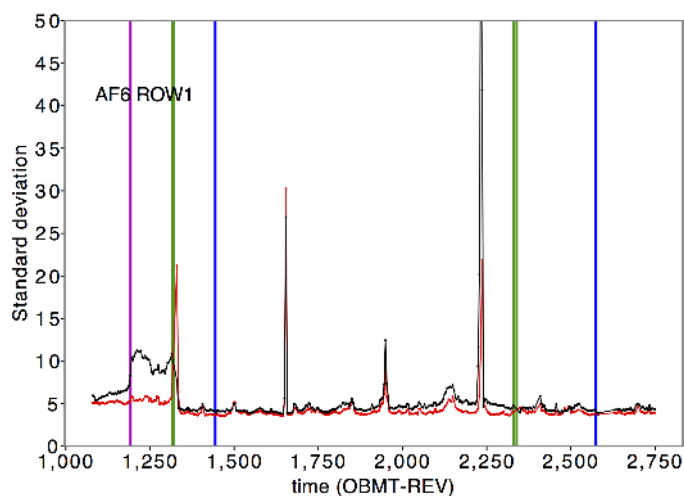


Fig. 10. Unit-weight standard deviation of the large-scale calibration as a function of time (in satellite revolutions) for an example calibration unit. In this case, AF6, Row 1, Window Class 1, No Gate. The black lines are for the preceding and red for the following FoV calibration units. The vertical lines represent significant satellite events: scanning law change (magenta), decontamination (green), and refocussing (blue).

it is not expected that the values found in the solutions would be close to ideal, either because the calibration model does not represent the systematics very well or because the quoted errors on the fluxes do not correctly represent the true error (or both). Figures 10 and 11 show example plots of the standard deviation for the large- and small-scale calibrations, respectively. Where the standard deviation varies from the average value, it indicates a region where the calibration model is worse at modelling the systematic effects and that a possible improvement or additional calibration feature is required. In the example of the large-scale calibration (Fig. 10), the average value of 5.0 implies that the observed scatter in the data for this configuration will be 5 times worse than the quoted errors for those periods with a standard deviation of 5.0. This only affects the individual transit measurements. It should be noted that the error on the weighted mean will not be affected by this since the measured scatter has been accounted for in its calculation (see Carrasco et al. 2016, for more details).

In the example shown for the large-scale calibration (Fig. 10), the peaks seen correspond to short periods, sometimes

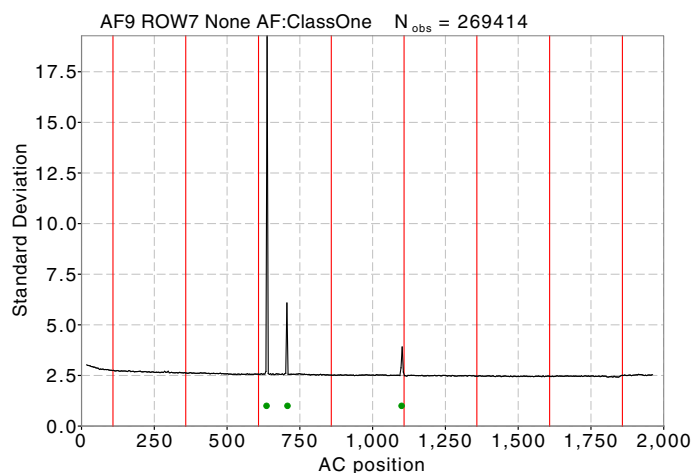


Fig. 11. Unit-weight standard deviation of the small-scale calibration as a function of across-scan position on the CCD for an example calibration unit. In this case, AF9, Row 7, Window Class 1, No Gate. The red lines show the locations of the CCD stitch blocks and the green dots show the location of detected bad columns.

individual calibrations, which indicate problems with the IPD (see Fabricius et al. 2016, for more details), such as the use of an incorrect or suboptimal LSF/PSF library. Future processing cycles will use redetermined IPD values for which many of these features will have been corrected. The period immediately after the first decontamination (within the period covered by *Gaia* DR1) may be problematic owing to the focal plane possibly not having reached thermal stability. The quality of these few days is being investigated further. Also seen in this plot is an indication that the period between the change in the scanning law and the first decontamination is of a poorer quality for the preceding FoV in comparison to the rest of the *Gaia* DR1 period. It should be noted that for *Gaia* DR1, the calibrations are carried out approximately every day, which is how time variation in the response function is calibrated.

For the small-scale calibration (Fig. 11), the main features seen in the standard deviation plots arise from bad columns. Many of these are confirmed in the CCD health calibrations (see Fabricius et al. 2016, for more details). In the later stages of the mission, this information will be used to mask the affected samples as part of the PSF fit of 2D windows performed by the IPD process (see Fabricius et al. 2016).

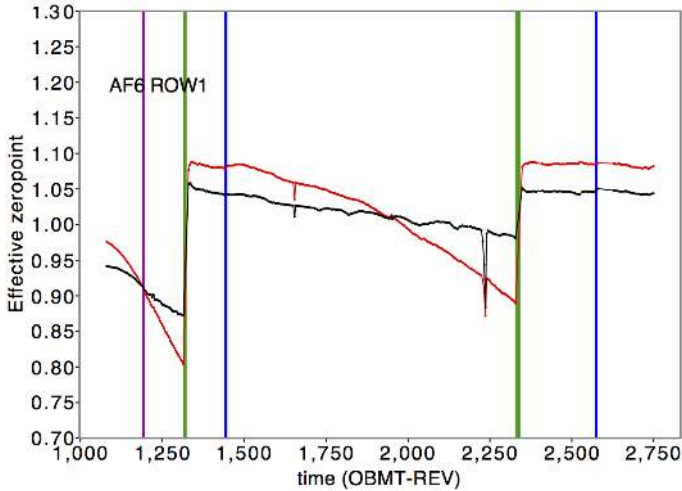


Fig. 12. Effective zeropoint of the large-scale sensitivity calibration as a function of time for an example calibration unit. The calibration unit is the same as in Fig. 10, as are the vertical lines. For this plot the SSC terms of the calibration model have been combined to form an effective zeropoint using default colours. This is necessary since there is no zeropoint term in the calibration model. See Carrasco et al. (2016) for more details.

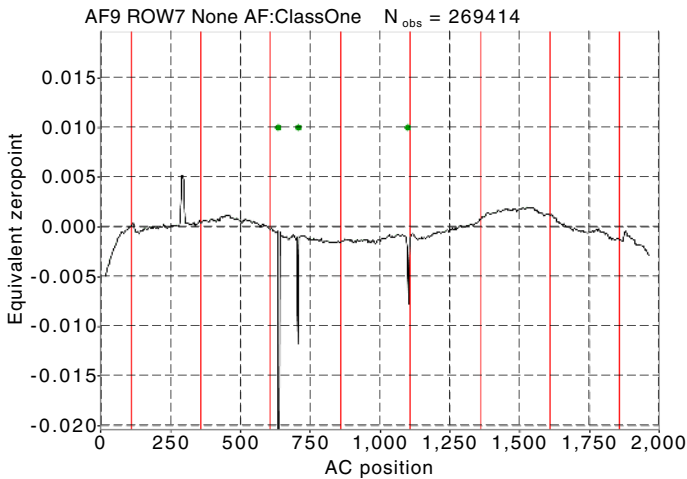


Fig. 13. Zeropoint of the small-scale sensitivity calibration as a function of across-scan position on the CCD for an example calibration unit. As defined in Carrasco et al. (2016), 1.0 has been subtracted from the zeropoint. The calibration unit is the same as in Fig. 11. The red lines show the locations of the CCD stitch blocks and the green dots show the location of detected bad columns.

Plotting the various calibration coefficients from the solutions as a function of time (LS) and AC position (SS) is also a good way to identify anomalies and to indicate where further investigation is required (see Figs. 12 and 13).

The main features seen in the large-scale calibration plots (Fig. 12) are the changes in the response of the CCD due to the varying levels of contamination on the mirrors and CCDs. As the mission progressed, more contaminant was deposited on the mirrors and CCDs, thus reducing the efficiency of the overall system. The response is different between the two FoVs; the mirrors associated with the following FoV are more highly contaminated. As already mentioned in Sect. 3, two decontamination campaigns were performed during the period covered by *Gaia* DR1. This successfully improved the photometric throughput as can be seen from Fig. 12. However, the contamination was not

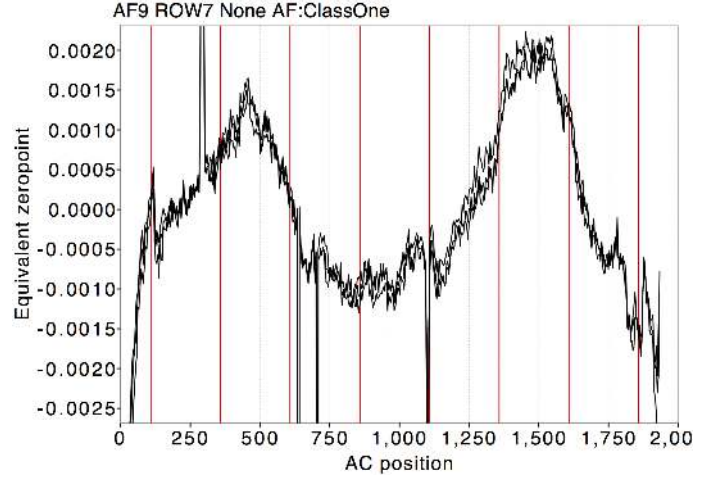


Fig. 14. Zeropoint of the small-scale sensitivity calibrations as a function of across-scan position on the CCD (same calibration configuration as Fig. 11) where the time range of *Gaia* DR1 has been divided giving three sets of calibrations. We note the change in the ordinate scale. This plot was derived from a preparatory processing run (OR5S3).

fully removed and continued to increase with time, albeit at a reduced rate. It should be noted that some of the spikes seen in the standard deviation plots (Fig. 10) are also seen in the coefficient plots (Fig. 12).

The main variation mapped out by the small-scale calibration is the response as a function of AC position on the CCD (Fig. 13). This is effectively a 1D flat field. Again, the bad columns present on the *Gaia* CCDs can be seen in the zeropoints of the small-scale calibrations. When combined with the matching standard deviation plot (Fig. 11), this shows that the current model is not appropriate for these columns. This plot shows also a small variation in the response at around AC position 300 for a small number of columns. In this case, there is no corresponding spike in the standard deviation plot indicating that the model is reasonably correct and that this does represent a genuine response variation.

It should be noted that for *Gaia* DR1, only a single set of SS calibrations spanning the entire time range was computed in order to ensure enough calibrators at the bright end of the magnitude scale. In order to verify that the SS calibrations are indeed stable over the entire time range, the period was divided into three and a set of calibrations was derived for each one. No significant variation was seen between the three sets of calibrations at the level that was required for *Gaia* DR1 (see Fig. 14). The variation in this plot, typical for Window Class 1 ($13 < G < 16$), was 0.17 mmag as measured by the robust width mentioned earlier.

6. Convergence of the large-scale calibrations

As described in Carrasco et al. (2016), the photometric system needs to be established in the initial stages of calibration. This is done by iterating between the large-scale calibration and determining the reference fluxes using the latest iteration of calibrations. In order to show that the system is converging, a form of convergence metric needs to be used. The one chosen was an L1 norm and was chosen in preference to the L2 norm since it is more robust to outliers. The general form of the L1 norm is

$$\int |p_i(\mathbf{x}) - p_{i+1}(\mathbf{x})| d\mathbf{x}, \quad (1)$$

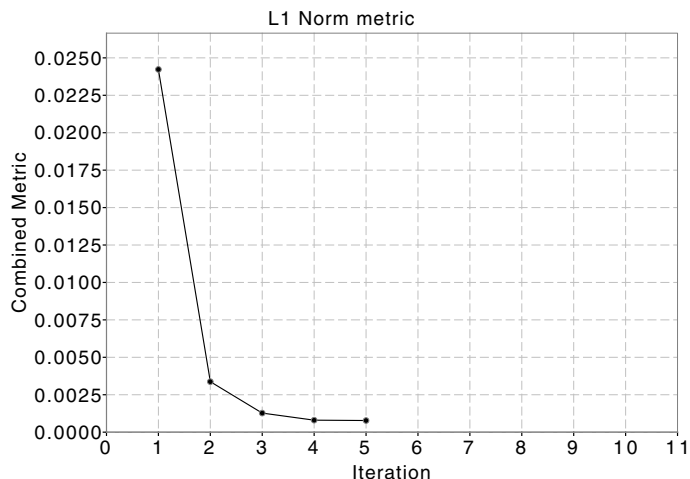


Fig. 15. Convergence metric as a function of iteration for the *G*-band Window Class 2 large-scale calibrations. These metrics compare the large-scale calibrations between two iterations, the one numbered in the plot and the following one. The exception is the final point which compares the large-scale calibrations at the end of the initial set of iterations and those done after the small-scale calibrations have been carried out; see Carrasco et al. (2016) and Riello et al. (in prep.) for more details.

where p_i corresponds to the calibration factor for the i th iteration and \mathbf{x} the singular parameters of a source. If this integral is carried out over a representative range of parameter space, the norm represents the typical change in the calibration factors when going from one iteration to the next. In this analysis, this was done by using the singular parameters (e.g. colour) of about 1000 randomly selected sources. The overall metric used was the median value of the norms for the calibrations considered.

Figure 15 shows the convergence metric for the *G*-band Window Class 2 calibrations ($G > 16$). The final data point shows the difference between the final LS calibrations of the iteration stage and the LS calibrations performed after the SS calibrations have been carried out. It can be seen that the photometric system converges very well. After five iterations were carried out, it was decided to stop the initialisation process considering that the changes had reached the mmag level. In future releases, further iterations will be carried out to improve on this performance.

7. Analysis of accumulation data

As described in Carrasco et al. (2016), the data for each source is accumulated and various statistics gathered. Figure 16 shows the distribution of the number of *G*-band CCD transits for each source analysed. To remove most of the spurious detections made by *Gaia*, which are mainly around bright sources, the validation analysis has a lower cut-off of 30 CCD transits (roughly corresponding to 3 FoV transits) as seen in this histogram. Because they are spurious, such detections are unlikely to be matched with other observations (see the section on cross-matches in Fabricius et al. 2016) and such “sources” will thus have low numbers of CCD transits accumulated. The average number of *G*-band CCD transits for *Gaia* DR1 is just under 100 (with mean and median equal to 97 and 79, respectively) which corresponds to about 10 FoV transits. The spread in the number of observations is due to the scanning law, and some sources will have significantly more observations than the average.

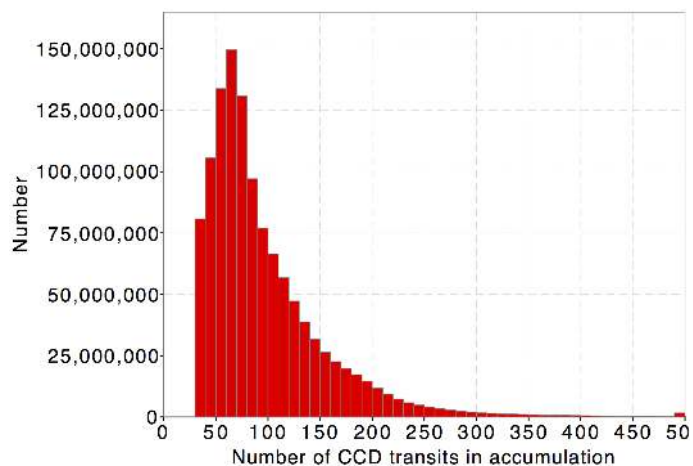


Fig. 16. Distribution of the number of *G*-band CCD transits for each source analysed.

The distribution of quoted error on the weighted mean¹ as a function of magnitude shown in van Leeuwen et al. (2017) cannot be compared with expectations because each source has a different number of observations. Figure 17 shows the same analysis, but is restricted to those sources with between 90 and 110 CCD transits. The results for these sources can then be compared with predictions for $N_{\text{obs}} = 100$ using the formulation given in Jordi et al. (2010). The lower line (green) gives the expected errors for a nominal mission and no calibration errors. The zig-zag variation at $G < 12$ shows the effect of gating which changes the effective exposure time of the observations. Adding a 3 mmag calibration error to this formulation shows the general level of calibration that has been achieved for *Gaia* DR1.

Further features can be seen in this figure.

At the faint end, the main difference between the nominal and current mission is the increased stray light level which leads to poorer performance than expected. This cannot be calibrated out since it is purely an increase in the noise level.

The jumps at approximately $G = 13$ and $G = 16$ are due to changes in the window Class which affect the IPD algorithm and the number of pixels present in the image window. It should be noted that they do not occur exactly at these magnitudes since the plots are made with calibrated photometry, which is different to the on-board magnitude estimates that were used to determine the configurations (gate and window class) for each observation.

The increase in error seen at $G = 16$ is linked to the change in the size of the window configuration. In the range $16 < G < 17$, a limit is reached in the accuracy, probably caused by IPD issues.

At $G = 13$, the window Class changes from 1D to 2D windows for the brighter transits and the IPD algorithm therefore changes (Fabricius et al. 2016). The greatest effect is that an AC LSF component is needed in the fitting. At this early stage of the mission, the best AC LSF to use is not very sophisticated and does not include colour or AC velocity dependencies. Although the colour will remain the same for each observation for most sources, the AC velocity will not. This means that an additional noise is introduced into the flux determination. Moreover, at this point the effect of flux loss affects observations fainter than $G = 13$. When initialising the photometric system from raw observations, care must be taken to make sure that

¹ The quoted error on the weighted mean includes a contribution from the measured scatter and thus accounts for any underestimation of the errors on the individual transits. See the section on the “Reference photometry update” in Carrasco et al. (2016).

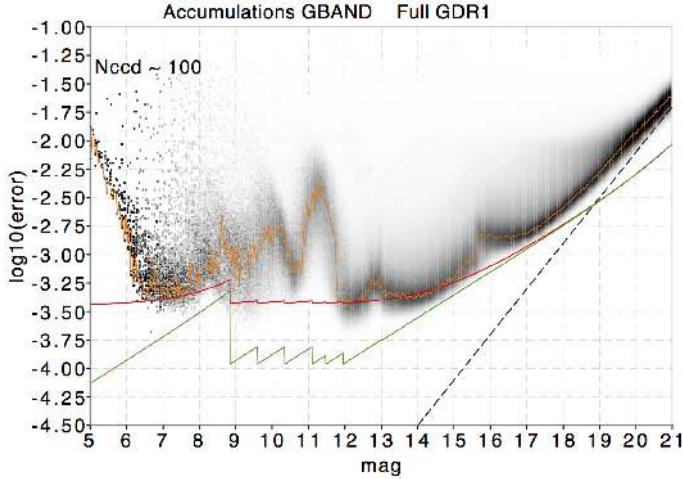


Fig. 17. Distribution of error on the weighted mean G -value as a function of magnitude. The orange line shows the mode of the distribution. This plot is restricted to all sources with between 90 and 110 CCD transits. The green line shows the expected errors for sources with 100 CCD transits and for a nominal mission with perfect calibrations. The red line shows the same error function, but with a calibration error of 3 mmag added in quadrature to the individual observations. The dashed black line has a slope of 0.4 and indicates that the faint end is sky dominated. The distribution has been normalised along the magnitude axis, i.e. scaled so that each magnitude bin has the same number of sources in order to show features along the whole magnitude range. The greyscale is linear.

discontinuities are not introduced into the system. This is described further in Sect. 4 in Carrasco et al. (2016). If there are problems with this calibration, then a larger scatter will be seen for sources around this magnitude.

At the bright end some of the increased scatter is caused by saturation. Setting the gate configuration at the time of observation should remove most of the saturation by changing the effective exposure time; however, the accuracy of the on-board determination of the source magnitude, which determines the gate configuration, is poor (about 0.3 mag) at the bright end (Gaia Collaboration 2016b). This means that some observations are carried out with a gate configuration that does not eliminate saturation. While some masking of saturated pixels is carried out by the IPD, the calibration library used for this purpose is an early version from the commissioning period which only accounts for numerical saturation. Updates of this library will be in place for the next release.

The other variations at the bright end are also caused by the different gate configurations being set. This changes the effective exposure time for each observation which alters the amount of smearing caused by the AC velocity. The amount of additional noise seen will depend on the AC LSF selected. At this stage of the mission, no variation in the AC LSF is made as a function of AC velocity (Fabricius et al. 2016).

From the accumulated data for each source, a P -value can be calculated from the χ^2 of the weighted mean flux calculation. This is defined as the probability that the transits that have been used in forming the weighted mean flux for each source are normally distributed about the mean according to their quoted errors, i.e. there is no additional source of noise, for example source variability.

The P -values can be calculated using the equation

$$P = Q\left(\frac{(n-1)}{2}, \frac{\chi^2}{2}\right), \quad (2)$$

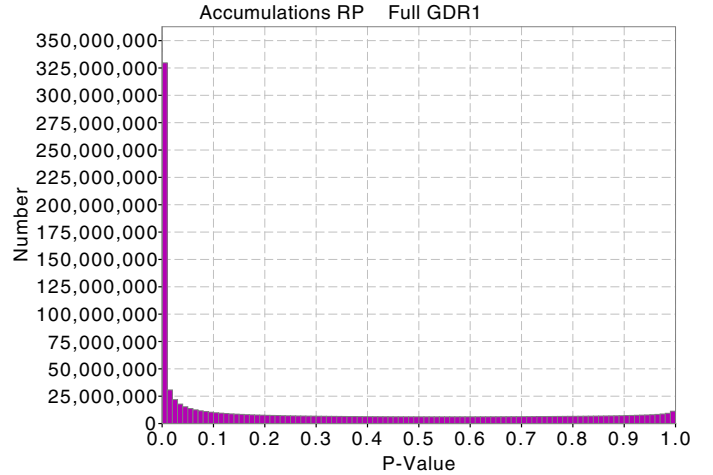


Fig. 18. P -value distribution for G_{RP} for the *Gaia* DR1 sources.

where Q is an incomplete gamma function (Press et al. 1993) and n the number of CCD transits.

If the quoted errors are accurate and representative, this is a very good way of detecting variability. However, this is not the case with the current G -band data and the quoted errors from the IPD do not account for model inaccuracies, such as using an LSF that is too simple in the IPD fit. This means that the CCD-level transits would be seen as having an underestimated quoted error. A consequence of this underestimation is that almost all sources have a G -band P -value of 0.0 and are seen as variable. Although no direct rescaling of the individual photometric errors is carried out for *Gaia* DR1, the calculation of the error on the weighted mean flux does take into account the scatter of the data and thus this error is realistic.

The situation is different for G_{BP} and G_{RP} since the flux determination is carried out using a simple integration rather than a model fit (Carrasco et al. 2016). The errors here have contributions from photon noise, background determination, and the geometric and differential dispersion calibrations. As can be seen from Fig. 18, the main feature in the P -value distribution for G_{RP} is the peak at 0.0, which either indicates variability or that the calibration model is not well matched to the data for these sources. The significant flat distribution between 0.0 and 1.0 indicates that the quoted errors are realistic. No such flat distribution was seen in the equivalent G -band analysis.

8. Analysis of the residuals

A detailed analysis of the residuals allows us to validate the correctness of the calibration models by showing that there are no systematic dependencies left from the calibration parameters after the application of the calibrations. In this case residuals are computed as the difference between the calibrated epoch magnitude and the reference magnitude for each source.

Each calibration unit is calibrated independently and therefore will naturally have residuals centred on zero. We have analysed residual distributions for all CCDs in various magnitude ranges, and indeed cannot see significant differences.

In particular, residuals do not show any significant dependency on the calibration parameter AC coordinate. Figure 19 shows one such distribution (for the case of the AF1 CCDs and for the window Class configuration nominally assigned to sources with magnitude $13 < G < 16$). This is representative of similar distributions in other locations on the focal plane.

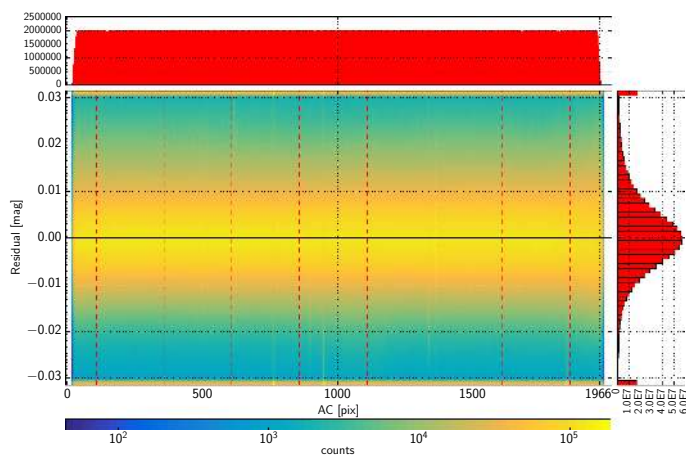


Fig. 19. Distribution of photometric residuals against the AC coordinate for all data in AF1 CCDs and Window Class 1 (assigned to sources with magnitude $13 < G < 16$ as estimated on board).

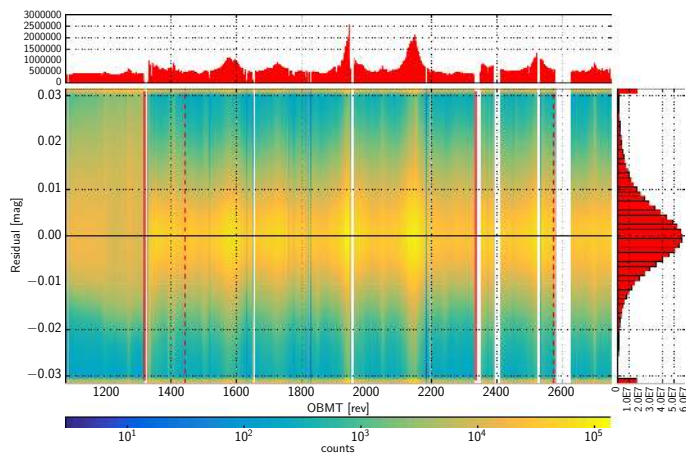


Fig. 20. Distribution of photometric residuals in time for all data in AF1 CCDs and Window Class 1 (assigned to sources with magnitude in the range $13 < G < 16$ as estimated on board). The time is given in OBMT revolutions (one revolution corresponds to approximately 6 h). Vertical solid red lines mark the occurrences of decontamination activities, while dashed lines correspond to refocus events.

In Fig. 20 the distribution in time of the residuals for the same CCDs and magnitude range used in Fig. 19 shows a non-Gaussian distribution of the residuals for the EPSL period where the data was heavily affected by contamination and poor LSF calibrations. From the first decontamination (marked by the first continuous vertical red line) onwards there is no sign of systematic problems in the residual distribution.

A sky map of the median photometric residual (as shown in Fig. 21 for the same set of observations used in other residual plots in this section) indicates that there are some areas of the sky and in particular some satellite scans that were not properly calibrated at the 0.01 mag level in the worst cases.

9. Analysis of data for mainly constant sources

One of the best ways of verifying the accuracy of the photometry is to carry out an analysis of constant sources. This makes the assumption that there is a population of non-variable sources and that they can be selected such that they do not bias the results. Various studies using HIPPARCOS and *Kepler* data have shown

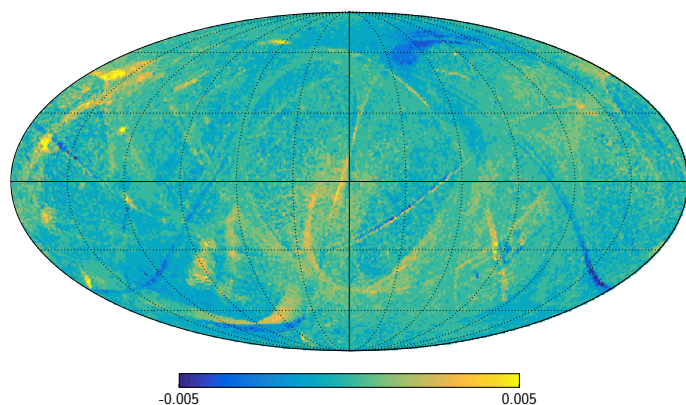


Fig. 21. Distribution of the median photometric residual in the sky for all data in AF1 CCDs and Window Class 1 (assigned to sources with magnitude in the range $13 < G < 16$ as estimated on board). The map is shown using equatorial coordinates in Mollweide projection.

that all stars are variable at some level, but this is at a very low level (Ciardi et al. 2011; Eyer & Grenon 1997).

Given a selection of constant sources, by measuring their observed scatter the accuracy of the photometry can be assessed and compared to expectations. For constant sources, the scatter is caused by the two factors affecting the accuracy of the photometry, random noise and calibration error. Because all sources are variable to some extent, the measured scatter will have a natural minimum value. Ciardi et al. (2011) showed that this was at the mmag level, but quite complicated in its dependency on stellar type. Since this gives a minimum value in a similar way to that of an unknown calibration error, it is very difficult to distinguish between the two. Comparisons between the results in G , G_{BP} , and G_{RP} can provide some information that can be helpful in distinguishing between the intrinsic variability of all sources and the calibration noise.

In the main part of the analysis of the photometry of these sources, a robust estimate of the scatter is made using the interquartile method mentioned earlier to estimate the standard deviation of the distribution. This is unaffected by photometric outliers which are likely to be present in this early reduction of the data.

As mentioned, care must be taken in selecting the constant sources. If the same scatter is used to exclude variables and to estimate the photometric accuracy, then the measured distribution will be biased and narrower than it truly is. In order to avoid this bias, it was decided that the analysis would be carried out on all sources since the majority of sources (>90%) do not have large amounts of variability (Eyer & Grenon 1997).

This particular analysis is restricted to sources in the most observed sky regions (which have a mean of about 300 CCD transits). In general, this restricts the sources to the ecliptic poles and the areas around ecliptic latitude $+45^\circ$ or -45° . These are areas that have been observed more often due to the scanning law of *Gaia*. A further random selection was carried out to reduce the number of faint sources such that there was a relatively flat distribution across the magnitude range.

Figure 22 shows the results from this analysis for the G band as a function of magnitude. Also shown in this plot are the expected accuracies as derived from the equations given in Jordi et al. (2010). The discontinuities are due to different observing configurations such as gates and window class, which are controlled as a function of magnitude as measured on board the satellite (Fabricius et al. 2016). Between $G = 16$ and 17,

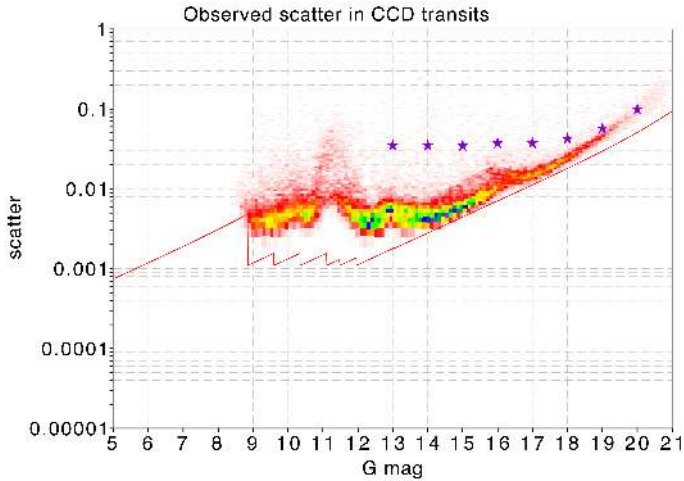


Fig. 22. Measured scatter in G for sources in the most observed sky regions as a function of magnitude. The line shows the predicted accuracies using the formulation given in Jordi et al. (2010). The star symbols are the expected accuracies given on the *Gaia* scientific performance web page.

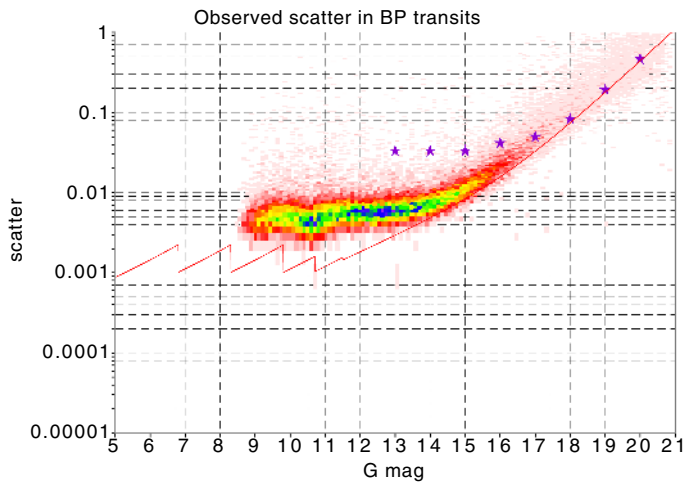


Fig. 23. As Fig. 22, but for G_{BP} .

there seems to be a plateau in the scatter distribution pointing to a possible accuracy limit. For sources brighter than $G = 16$, additional samples are transmitted by *Gaia*, the accuracy improves and is closer to the expected values. Other features can be seen at the bright end and are consistent with the features seen in the results from the accumulations (see Fig. 17). The plot in Fig. 22 shows the scatter on CCD transits, while Fig. 17 shows the error on the weighted mean for sources with about 100 CCD transits and thus accounts for the factor of 10 difference between them.

Toward faint magnitudes, the distribution of the data seems to follow sky-dominated Poisson statistics at a level higher than expected. This is probably due to residual problems related to the stray light calibration for the G -band measurements. Results at the faint end for BP and RP (see Figs. 23 and 24) show a much better agreement with the expectations, thus confirming that the stray light calibration has successfully removed the effect of this additional background component on the integrated BP and RP photometry. It is worth reminding the reader that the G -band data enters the photometric calibration process in the form of image parameters, where the background calibration has already been computed and applied upstream (Fabricius et al. 2016), while for BP and RP the raw data is used.

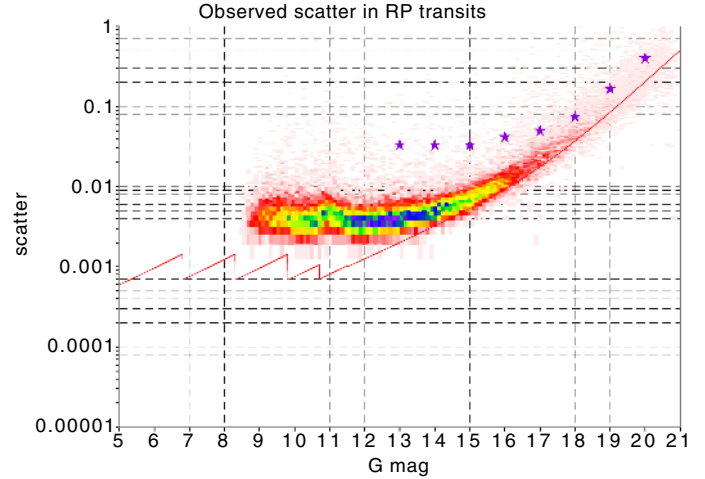


Fig. 24. As Fig. 22, but for G_{RP} .

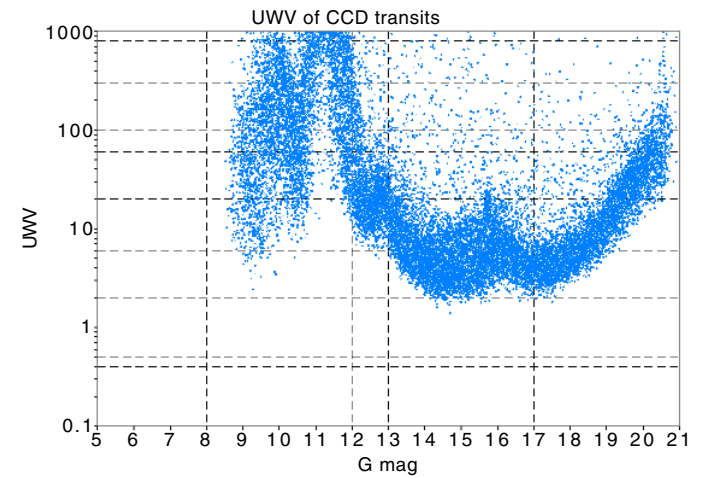


Fig. 25. Unit-weight variance as a function of magnitude for G .

Figure 22 also shows the expected accuracies as given on the *Gaia* scientific performance web page². These values reach a limiting accuracy at the bright end and are due to assuming a calibration error of 30 mmag. From this plot, it can be seen that a better performance has already been achieved and the limiting accuracy is about 3 mmag. This is still higher than the expected accuracy due to photon noise and it is foreseen that the performance will improve in future data releases as a better IPD is carried out and more complexity is added to the calibrations.

Figures 23 and 24 show the results for G_{BP} and G_{RP} . The limiting accuracies reached for these passbands are 3–4 mmag, similar to the G -band value. It should also be noted that these passbands are less affected at the bright end by saturation effects.

An analysis that can be done on the same sample of sources to validate the errors estimated by the IPD (Fabricius et al. 2016) is to investigate the unit-weight variance (Fig. 25). In this case, the variance or scatter is calculated with respect to the quoted error for each observation. The expected distribution should be centred around 1.0. This is not the case for this sample of sources as can be seen from Fig. 25. Large unit-weight variances can be due to variability of the source, uncalibrated systematics, or underestimated quoted errors. Results from previous analyses, in which comparisons were carried out with respect to expected

² <http://www.cosmos.esa.int/web/gaia/science-performance#photometric%20performance>

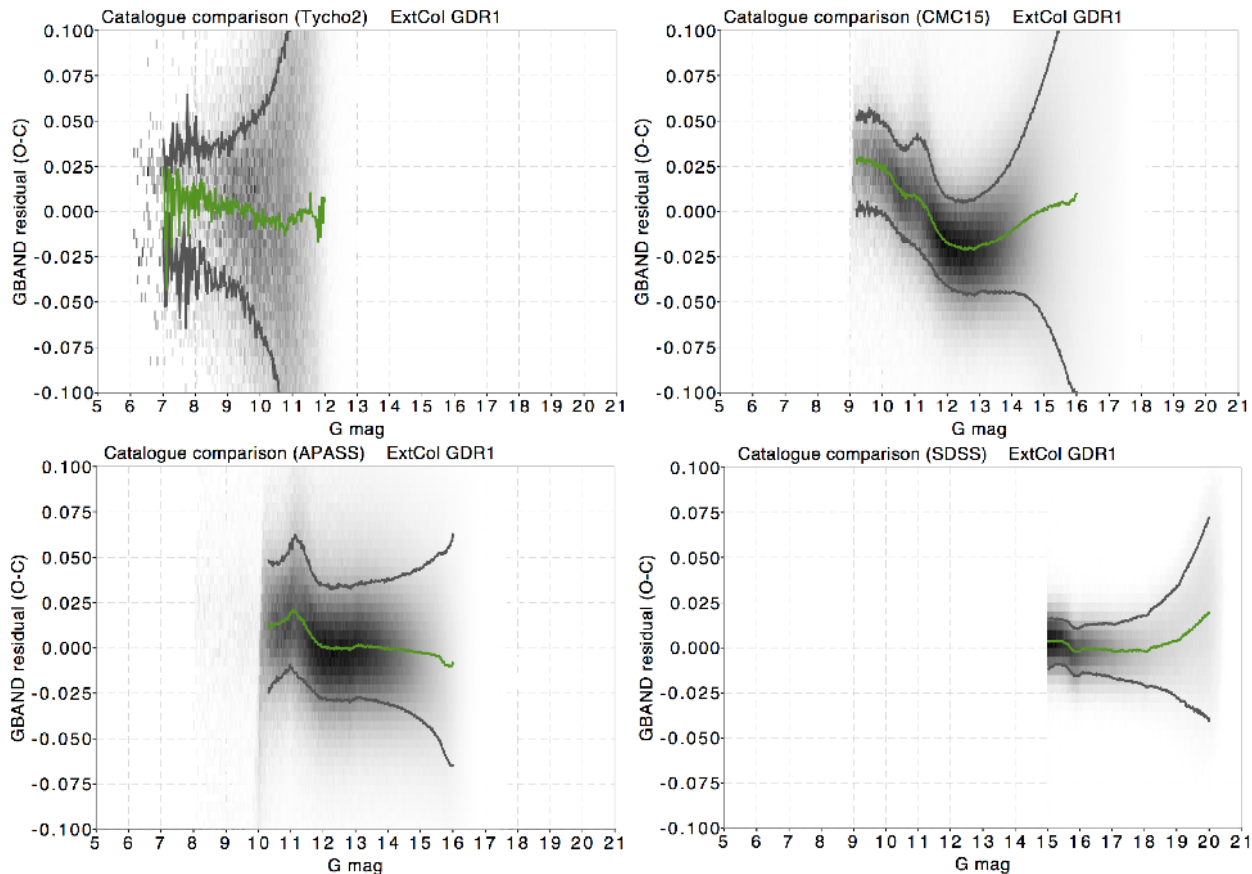


Fig. 26. Comparisons with respect to the external photometric catalogues: *Tycho* 2, CMC15, APASS, SDSS. The comparisons were carried out with respect to the r' passbands in all cases except for the *Tycho* comparison where the V_T passband was used. The green and black lines show respectively the median and one sigma points of the residual distributions. The greyscale is linear.

accuracies, show that there is not much additional scatter (due to variability or uncalibrated systematics). Therefore, we conclude that the quoted errors on the CCD-level transits are underestimated. It is expected that this will improve with later IPD results in future processing cycles thanks to a better determination of the LSFs. However, the issue may not be fully resolved for the very brightest sources.

10. Comparisons with external catalogues

Another way of validating results is to compare the data with other catalogues. The implied assumption with this approach is that the external catalogue is more reliable in some way than the data under test. For *Gaia*, this is usually not the case. The accuracy expected from the photometry will be much better than most external catalogues. Most of these catalogues will also not be all-sky and will contain systematic errors of some sort. Another issue that complicates comparisons is that the angular resolution for *Gaia* is much better than seen in any ground-based catalogue. This will cause many outliers when comparing areas of high source density such as the Galactic plane. For this reason, sources with $|b| < 10^\circ$ are excluded from this analysis.

Comparisons have been done with respect to the following external photometric catalogues: *Tycho* 2 (Høg et al. 2000), CMC15 (Muñoz & Evans 2014), APASS (Henden et al. 2015), and SDSS DR12 (Alam et al. 2015). The results of these comparisons are shown in Fig. 26. In order to perform such comparisons, the passband of the external catalogue needs to be converted to the one used by *Gaia*. This is complicated by issues

of absorption and luminosity class. This problem is avoided by restricting the colour range of the comparison and by positioning this narrow range such that the difference between G and the passband being compared is constant, thus making a direct comparison possible. The range also has to be selected such that there is a reasonable population of sources present to analyse. In this comparison, the range chosen was $1.0 < G_{BP} - G_{RP} < 1.2$. A single zeropoint offset is then determined for each catalogue to facilitate comparison.

The analysis of the distribution widths of these comparisons to validate the quoted errors is unreliable and difficult to interpret; the quoted errors of the external catalogues often refer to different magnitude ranges than the ones where the comparison distributions are narrowest. The quoted errors on the external catalogue are reasonably close to the minimum standard deviation in the comparisons, but no firm conclusions can be drawn from this.

The four catalogues chosen cover different magnitude ranges. The most useful catalogues to use are CMC15 and APASS since they approximately cover the same magnitude range and are of similar accuracies. When anomalies are seen in the comparisons, it is difficult to assess whether the problem lies in the *Gaia* photometry or in the external catalogue. If an anomaly is seen in more than one external catalogue comparison, it is likely that the issue is with the *Gaia* photometric results. This is especially the case if a plausible cause can be found. During the early reductions of the data, a jump was found at $G = 13$ in both these comparisons which corresponds

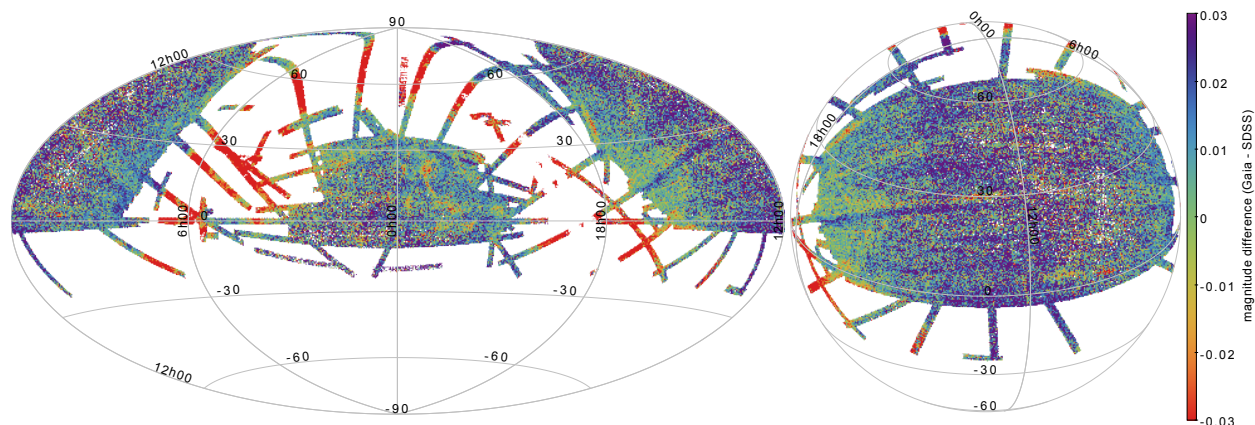


Fig. 27. Sky distribution of the median zeropoint between the *Gaia* and SDSS photometric catalogues. The comparison is limited to sources fainter than $G = 15$ and to sources in the colour range $0.8 < g - r < 1.1$. The empirical photometric transformations from van Leeuwen et al. (2017) have been used to estimate G magnitudes from g and r . The entire sky in equatorial coordinates is shown on the left, while the plot on the right shows a 3D view centred on the large area outside the Galactic plane covered by SDSS.

to a window class change in *Gaia*. This anomaly was dealt with by the Gate/Window Class link calibrations. See Carrasco et al. (2016) for more details. The plots in Fig. 26 show that this issue has been resolved.

These two comparisons also show one of the problems linked with this type of analysis. At the bright end of the CMC15 comparison there seems to be a magnitude term. Since this is not seen in the APASS results, this difference is likely to be in the CMC15 photometry. A reason for this deviation could be the asymmetrical images that occur away from the equator and that might cause problems for the isophotal corrections carried out in this catalogue (Evans et al. 2002). However, the bump of order 0.01 mag at $G = 11$ is likely to be in the *Gaia* data and might be caused by saturated images (also see Sect. 7).

Although the accuracy of the *Tycho 2* photometry is much worse than that of *Gaia*, a comparison with that catalogue is useful as it covers the brighter sources and shows rather good linearity. The SDSS comparison checks the fainter end of the magnitude range and shows that there are no large-scale anomalies. The slightly positive differences at the faint end can be real trends or can be incompleteness of the *Gaia* data due to the magnitude detection threshold. It should be noted that the SDSS comparison is limited to levels fainter than $G = 15$ owing to saturation effects in the SDSS photometry (York et al. 2000).

A plot of the sky distribution of the magnitude zeropoint between the *Gaia* and SDSS catalogues is shown in Fig. 27. In order to have a good coverage of the regions of the sky observed by SDSS, the selection in colour has been relaxed to $0.8 < g - r < 1.1$ and the empirical photometric transformations from van Leeuwen et al. (2017) have been applied to minimise the colour effects. Figure 27 shows the entire sky in equatorial coordinates in Hammer-Aitoff projection (left) and a view of the large area outside the Galactic plane covered by SDSS (right). The Galactic plane stands out with larger differences between the *Gaia* and SDSS magnitudes. Outside the Galactic plane the most prominent feature is the SDSS scanning pattern thus showing that the SDSS photometry dominates the error budget.

11. Conclusions

This paper has described the internal validation investigations on the photometry carried out for the first *Gaia* data release. Although only G -band photometry is present in *Gaia* DR1, some validation of the G_{BP} and G_{RP} photometry is shown since it is used in some of the G -band calibrations. In general, the

photometric calibrations have been carried out to the 3–4 mmag level, but there are systematics at the 10 mmag level at $G = 11$.

Acknowledgements. This work has been supported by the UK Space Agency, the UK Science and Technology Facilities Council. The research leading to these results has received funding from the European Community’s Seventh Framework Programme (FP7-SPACE-2013-1) under grant agreement No. 606740. This work was supported in part by the MINECO (Spanish Ministry of Economy) – FEDER through grant ESP2013-48318-C2-1-R and MDM-2014-0369 of ICCUB (Unidad de Excelencia “María de Maeztu”). We also thank the Agenzia Spaziale Italiana (ASI) through grants ARS/96/77, ARS/98/92, ARS/99/81, I/R/32/00, I/R/117/01, COFIS-OF06-01, ASI I/016/07/0, ASI I/037/08/0, ASI I/058/10/0, ASI 2014-025-R.0, ASI 2014-025-R.1.2015, and the Istituto Nazionale di Astrofisica (INAF). The work was supported by the Netherlands Research School for Astronomy (NOVA) and the Netherlands Organisation for Scientific Research (NWO) through grant NWO-M-614.061.414. This research has made use of the APASS database, located at the AAVSO web site. Funding for APASS has been provided by the Robert Martin Ayers Sciences Fund.

References

- Alam, S., Albareti, F. D., Allende Prieto, C., et al. 2015, *ApJS*, **219**, 12
- Arenou, F., Luri, X., Babusiaux, C., et al. 2017, *A&A*, **599**, A50 (Gaia SI)
- Carrasco, J. M., Evans, D. W., Montegriffo, P., et al. 2016, *A&A*, **595**, A7 (Gaia SI)
- Ciardi, D. R., von Braun, K., Bryden, G., et al. 2011, *AJ*, **141**, 108
- ESA, 1997, The HIPPARCOS and Tycho catalogues. Astrometric and photometric star catalogues derived from the ESA HIPPARCOS Space Astrometry Mission, ESA SP, 1200
- Evans, D. W., Irwin, M. J., & Helmer, L. 2002, *A&A*, **395**, 347
- Eyer, L., & Grenon, M. 1997, in HIPPARCOS - Venice ’97, eds. R. M. Bonnet, E. Høg, P. L. Bernacca et al., *ESA SP*, **402**, 467
- Eyer, L., Mowlavi, N., Evans, D. W., et al. 2016, *A&A*, submitted (Gaia SI)
- Fabrizius, C., Bastian, U., Portell, J., et al. 2016, *A&A*, **595**, A3 (Gaia SI)
- Gaia Collaboration (Brown, A. G. A., et al.) 2016a, *A&A*, **595**, A2 (Gaia SI)
- Gaia Collaboration (Prusti, T., et al.) 2016b, *A&A*, **595**, A1 (Gaia SI)
- Henden, A. A., Levine, S., Terrell, D., & Welch, D. L. 2015, in *AAS Meeting Abstracts*, **225**, #336.16
- Høg, E., Fabrizio, C., Makarov, V. V., et al. 2000, *A&A*, **355**, L27
- Jordi, C., Gebran, M., Carrasco, J. M., et al. 2010, *A&A*, **523**, A48
- Muñoz, J. L., & Evans, D. W. 2014, *Astron. Nachr.*, **335**, 367
- Press, W. H., Teukolsky, S. A., Vetterling, W. T., & Flannery, B. P. 1993, *Numerical Recipes in FORTRAN; The Art of Scientific Computing*, 2nd edn. (New York, USA: Cambridge University Press)
- van Leeuwen, F., 2007, HIPPARCOS, the New Reduction of the Raw Data, *Astrophys. Space Sci. Lib.*, **350**
- van Leeuwen, F., Evans, D. W., De Angeli, F., et al. 2017, *A&A*, **599**, A32 (Gaia SI)
- York, D. G., Adelman, J., Anderson, Jr., J. E., et al. 2000, *AJ*, **120**, 1579

Appendix A: Nomenclature

Table A.1. Below, we give a list of acronyms and useful concepts used in this paper.

Acronym	Description
AC	ACross scan: direction on the focal plane perpendicular to the scan direction
AF	Astrometric Field: the 62 astrometric CCDs on the focal plane
APASS	AAVSO Photometric All-Sky Survey
BP	Blue Photometer: the system containing the blue dispersion prism. Also refers to the associated CCDs
CCD	Charge-coupled Device
CCD transit	Transit of a source across a single CCD
CMC15	Carlsberg Meridian Catalogue, Number 15
EPSL	Ecliptic Pole Scanning Law: the scanning law of the satellite, where it is pointing as a function of time, during the first month of observations. See Gaia Collaboration (2016b) for more details on the various scanning laws of <i>Gaia</i>
ESA	European Space Agency
FoV	Field of View: one of the two pointing directions of the satellite telescopes. See (Gaia Collaboration 2016b) for more information regarding the structure of <i>Gaia</i>
FoV transit	Field-of-view transit, the complete transit of a source across the focal plane
IPD	Image Parameter Determination: the task that generates the fluxes that are calibrated as described in Carrasco et al. (2016) . This task also generates the raw astrometry. See Fabricius et al. (2016) for more details
LS	Large-scale: usually referred to in the context of the relevant photometric calibration
LSF	Line Spread Function
OBMT	On-board Mission Timeline: the timescale usually used when referring to time in the <i>Gaia</i> context. This scale is defined in Gaia Collaboration (2016b)
RP	Red Photometer: the system containing the red dispersion prism. Also refers to the associated CCDs
SDSS	Sloan Digital Sky Survey
SS	Small-scale: usually referred to in the context of the relevant photometric calibration
SSC	Spectrum Shape Coefficient: equivalent of a medium-band colour. These are defined in Carrasco et al. (2016)
TDI	Time-delayed Integration (CCD)